JOURNAL OF SPACECRAFT AND ROCKETS
Vol. 49, No. 4, July–August 2012

Flexible Launch Vehicle Stability Analysis Using Steady and Unsteady Computational Fluid Dynamics

Robert E. Bartels*
NASA Langley Research Center, Hampton, Virginia 23681

DOI: 10.2514/1.A32082

Launch vehicles frequently experience a reduced stability margin through the transonic Mach number range. This reduced stability margin can be caused by the aerodynamic undamping one of the lower-frequency flexible or rigid-body modes. Analysis of the behavior of a flexible vehicle is routinely performed with quasi-steady aerodynamic line loads derived from steady rigid aerodynamics. However, a quasi-steady aeroelastic stability analysis can be unconservative at the critical Mach numbers, where experiment or unsteady computational aeroelastic analysis show a reduced or even negative aerodynamic damping. A method of enhancing the quasi-steady aeroelastic stability analysis of a launch vehicle with unsteady aerodynamics is developed that uses unsteady computational fluid dynamics to compute the response of selected lower-frequency modes. The response is contained in a time history of the vehicle line loads. A proper orthogonal decomposition of the unsteady aerodynamic line-load response is used to reduce the scale of data volume and system identification is used to derive the aerodynamic stiffness, damping, and mass matrices. The results are compared with the damping and frequency computed from unsteady computational aeroelasticity and from a quasi-steady analysis. The results show that incorporating unsteady aerodynamics in this way brings the enhanced quasi-steady aeroelastic stability analysis into close agreement with the unsteady computational aeroelastic results.

Nomenclature

$[A_0]$ = Roger approximation aerodynamic stiffness matrix
$[A_1]$ = Roger approximation aerodynamic damping matrix
$[A_2]$ = Roger approximation aerodynamic apparent mass matrix
$[B_{\text{cfd}}]$ = projection matrix, structure to computational fluid dynamics surface nodes
$[B_{\text{ll}}]$ = projection matrix, structure to line-load analysis points
$\{C\}$ = vector of x, y, and z nondimensional line loads
C_{xn} = x-direction nondimensional line load at station n
D_{ref} = reference diameter, in.
$\{G\}$ = generalized force
$\{\hat{G}\}$ = Fourier transform of generalized force
$\{g\}$ = generalized variable
$[M]$ = structural and aerodynamic mass matrix
$[\hat{Q}]$ = Fourier transform of generalized force per unit generalized variable
$[Q_k]$ = aerodynamic stiffness matrix
$[Q_m]$ = aerodynamic apparent mass matrix
$[Q_\zeta]$ = aerodynamic damping matrix
q_{nom} = nominal trajectory freestream dynamic pressure, lb/in.^{2}
q_∞ = freestream dynamic pressure, lb/in.^{2}
S_{ref} = reference area, in.^{2}
V_∞ = freestream velocity, in./s
α = angle of attack, deg.
γ = Roger approximation lag root
$[\Delta]$ = structural and aerodynamic damping matrix
$\{\delta\}$ = aeroelastic displacement vector, in.
ζ_a = aerodynamic damping ratio
$\{\xi\}$ = unsteady aerodynamic lag state
$[\Phi_{\text{cfd}}]$ = modal vectors projected to the computational fluid dynamics surface mesh
$[\Phi_{\text{ll}}]$ = modal vectors projected to the line-load analysis points
$[\Phi_{\text{POD}}]$ = unsteady aerodynamic proper orthogonal decomposition modal vector
$[\phi]$ = matrix of eigenvectors of structural dynamic equations
$\{\chi\}$ = state variable
$[\Omega]$ = structural and aerodynamic stiffness matrix

Subscripts

dd = dynamic aerodynamics on dynamic mode submatrix
ds = dynamic aerodynamics on static mode submatrix
ll = line loads
sd = static aerodynamics on dynamic mode submatrix
ss = static aerodynamics on static mode submatrix

I. Introduction

THE Ares program was given the task to develop a vehicle to launch the crew capsule and associated hardware to destinations beyond low earth orbit. The engineering of the Ares Crew Launch Vehicle (CLV) or follow on vehicles is a departure from the past in that computational fluid dynamics (CFD) will be an integral part of the design from the conceptual stage. Future vehicles can be expected to be designed with a smaller proportion of aerodynamic data derived from wind-tunnel testing and increasing amount from computational fluid dynamics [1]. An increased portion of data produced by CFD poses both exciting possibilities in the extent to which the flowfield physics of a launch vehicle can be understood as well as challenges in validating methodologies for the highly complex flowfield about a launch vehicle.

One of the notable features of the Ares CLV is the use of a five-segment solid rocket booster (SRB) as a first stage with a larger-diameter upper stage. The two stages are connected by an aft-facing interstage frustum. Along with the usual geometric complexity of protuberances over a major launch vehicle, this hammerhead configuration poses a challenge to CFD because it has the potential of producing flowfield separation from the frustum. A combined shock

Presented as Paper 2011 at the AIAA Aerospace Sciences Meeting, Orlando, FL, 4–7 January 2011; received 5 April 2011; revision received 11 July 2011; accepted for publication 12 July 2011.

*Senior Aerospace Engineer, Aeroelasticity Branch, Mail Stop 340. Senior Member AIAA.

and frustum separation can significantly influence overall vehicle aerodynamics [2–4]. The extent of separated flow over the Ares vehicle has motivated the use of a high-fidelity Navier–Stokes solver and a model of the structural dynamics coupled aeroelastically.

Aeroelastic stability has been a concern since early development of the Saturn I [5,6]. Vehicles with a hammerhead configuration, having a larger-diameter upper stage, have the potential for aeroelastic instability [2,3]. The potential for significant shock separation dynamics over a conical forebody and boattail flow separation is well known. The SRB aft skirt adds an additional mechanism for dynamic aeroelastic instability due to the disturbance time lag between the upper stage, interstage frustum and the aft skirt [2]. The time lag due to flow separation and reattachment has the potential to couple with vehicle flexibility [4]. Furthermore, launch vehicle experience indicates that low-frequency modes are particularly susceptible to coupling with such large scale unsteady flow structures. For instance, analyses of the Delta II and the Saturn I included only the first few low-frequency modes [3,5–7]. In reproducing the Atlas-Able IV flight aeroelastic instability, Azevedo [8] calculates it to involve the second mode. Analysis by Reding and Ericsson [9] indicates that the Seasat-A to be launched on an Atlas/Agena booster had the possibility of a coupling between the third structural mode and aerodynamic undamping. Recent computational aeroelastic simulations of the Ares I included many modes; however, only the first two bending modes coupled closely with the flowfield [10]. In each of the examples above, the mode in question was a lower-frequency bending mode. Ericsson [4] indicates that, as a general rule, most (if not all) of the flexible response to aerodynamic undamping is by the first several bending modes. Furthermore, negatively damped low-frequency modes have the potential to couple with rigid-body dynamics and degrade overall vehicle controllability.

The standard method to simulate flexible launch vehicle dynamics is to use steady rigid line loads [2,3,6,11], commonly called the quasi-steady method of line loads. This will be denoted here as the flexibilized rigid integrated line loads (FRILLS) method. This quasi-steady approach models the displacement and inertial, elastic, and aerodynamic forces by a distribution along the vehicle centerline axis. The aerodynamic forcing is usually derived from steady-state rigid aerodynamics, either from wind-tunnel surface pressures, slender-body theory, or CFD. This model is based upon the assumption that, unlike lifting surfaces, the loading of a slender flexible launch vehicle can be approximated by assembling line loads at local angles of attack that were computed from rigid steady CFD. The limitation of the quasi-steady aeroelastic method of line loads is that it does not represent a true aeroelastic interaction of a vehicle in flight. The use of rigid steady aerodynamics assumes that each station along the body is influenced only by local angle of attack and is not in any way influenced by flexibility-induced downwash from upstream or downstream aerodynamic response to flexibility. Vehicle dynamics simulated by the quasi-steady aerodynamic method is further removed from reality, unless the model is enhanced by additional states to account for the phase shift due to the unsteady flow.

Although the FRILLS method is convenient, very versatile, and therefore still frequently used, unsteady aeroelastic CFD launch vehicle analysis has been steadily expanding over the last several decades [8,10,12–16]. The use of a nonlinear aeroelastic Reynolds-averaged Navier–Stokes (RANS) solver is still rare, however, because it is computationally expensive. For this reason, there is a move toward incorporating unsteady aerodynamic effects through CFD system identification within a reduced-order state-space model. Along this line, Capri et al. [17] use system identification of inviscid aerodynamics to perform aeroelastic stability analysis of the VEGA European small launch vehicle. Silva et al. [18] perform system identification to extract a state representation of the unsteady aerodynamics of the NASA Ares I CLV and Ares I-X flight-test vehicle. In each of these cases the expense of simulating a flexible launch vehicle is mitigated by the use of reduced-order modeling. The only additional expense of an unsteady state-space model over the quasi-steady model is the inclusion of unsteady aerodynamic states and the pulse/response required to obtain them.

The examples just cited performed a system identification of all modes used in the aeroelastic analysis. If it is possible to add unsteady aerodynamic states only to those associated with the lowest-frequency modes, it may be possible to limit the computational expense of the pulse/response. It also may be possible to limit the size of the state-space model required. In this way, the aeroelastic state-space simulation can be performed combining the unsteady aerodynamics of the first few modes with a quasi-steady modeling of the higher-frequency modes and/or rigid-body modes. Furthermore, an extraction of unsteady line loads rather than generalized force–time histories makes that data compatible with the steady line-load data.

With the potential of these advantages, the purpose of the present study is to outline an approach to accomplish a flexible launch vehicle analysis that judiciously combines steady and unsteady CFD. Previous aeroelastic analysis was presented of the Ares I A105 CLV using the unstructured RANS code FUN3D (Fully Unstructured Navier–Stokes Three-Dimensional). The structural representation of the vehicle was introduced by use of a normal modes analysis from the finite element model of the vehicle. Reference [10] presents a comparison of the modal aerodynamic damping at Mach 1 and $\alpha = 0$ deg from the FRILLS method with a time-marching aeroelastic analysis using FUN3D. Those results are reproduced in the present paper in Fig. 1. The higher-fidelity unsteady FUN3D aeroelastic analysis showed the aerodynamics of the first mode is significantly undamped for the thrust oscillation isolator (TOI) structural model. The lower-fidelity FRILLS method produced a first-mode aerodynamic damping that was significantly positive. The FRILLS analysis is thus unconservative at the critical Mach 1 condition, since it indicates much more aerodynamic damping than the unsteady aeroelastic simulation. The present paper provides a way to enhance the FRILLS method by combining steady and unsteady line loads to produce the correct aerodynamic damping.

II. Methods of Analysis

A. FUN3D Aeroelastic Solver

The Navier–Stokes code used in this study is FUN3D. The FUN3D flow solver is a finite volume unstructured CFD code for either compressible or incompressible flows [19,20]. In the present study the RANS solver and the loosely coupled Spalart–Allmaras turbulence model are used on an all-tetrahedron grid [21]. The low-dissipation flux-splitting scheme for the inviscid flux construction and the blended van Leer flux limiter [22] were used. The solution at each time step is updated with a backward Euler time-differencing scheme and the use of local time-stepping. At each time step, the linear system of equations is approximately solved either with a multicolor point-implicit procedure or an implicit line-relaxation scheme [23]. Domain decomposition exploits the distributed high-performance computing architectures that are necessary for the grid sizes used in the present study. Additional details and source

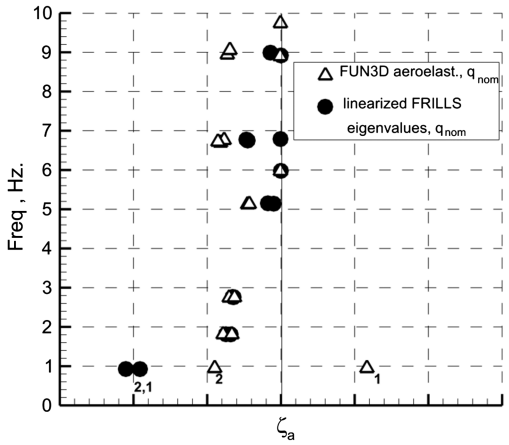

Fig. 1 Frequency versus damping due to the unsteady FUN3D and quasi-static FRILLS analyses [10].

references regarding the mesh deformation scheme and the aeroelastic formulation in FUN3D are discussed elsewhere [10].

B. Dynamic Aeroelastic Analysis Based on Line Loads Including Unsteady Aerodynamic Effects

A review of the method of line loads for launch vehicles is presented in a paper by Bartels et al. [10], denoted there as the FRILLS method. The vehicle is partitioned into N_{ll} stations along the vehicle axis. Modal analysis of the finite element model provides mode shapes that are projected to these stations. The projection can be written

$$[\Phi_{ll}] = [B_{ll}][\phi] \tag{1}$$

where $[B_{ll}]$ is a $3N_{ll} \times 3N_s$ projection matrix relating structural and line-load analysis centerline nodes, and $[\Phi_{ll}]$ is a $3N_{ll} \times N_{n\text{modes}}$ matrix of mode shapes projected to the line-load analysis centerline nodes. The matrices $[B_{ll}]$ and $[B_{\text{cfd}}]$) use the same method of projection to ensure consistency of the line-load results and the FUN3D CAE results. The modal transformation yields

$$\{g\} = [\phi]^T [B_{ll}]^T \{\delta\} \tag{2}$$

The vector of line loads at time step l is

$$\{C\}_l = \{\, (C_{x1})_l \quad (C_{y1})_l \quad (C_{z1})_l \quad \cdots \quad (C_{xN_{ll}})_l \quad (C_{yN_{ll}})_l \quad (C_{zN_{ll}})_l \,\}^T \tag{3}$$

and isolating the x-direction line loads, for instance,

$$\{C_x\}_l = \{\, (C_{x1})_l \quad \cdots \quad (C_{xN_{ll}})_l \,\}^T \tag{4}$$

The aerodynamic loading at each body station n, C_{xn}, C_{yn}, and C_{zn} are functions of Mach number, angle of attack, and angle of sideslip. The line-load aerodynamics are computed by integrating pressure coefficients at the vehicle surface from the FUN3D solution using the method of [24].

The linearized structural dynamics equation can be written

$$[M]\{\ddot{g}\} + [\Delta]\{\dot{g}\} + [\Omega]\{g\} = 0 \tag{5}$$

where

$$[M] = I - \rho_\infty [Q_m], \qquad [\Omega] = [\omega^2] - \rho_\infty V_\infty^2 [Q_k]$$
$$[\Delta] = [2\zeta_{\text{sd}}\omega] - \rho_\infty V_\infty [Q_\zeta] \tag{6}$$

In the quasi-steady formulation of [10] the apparent aerodynamic mass $[Q_m] = 0$. Here, apparent mass terms arise from the Roger approximation to be discussed subsequently. The aerodynamic stiffness $[Q_k]$ and damping $[Q_\zeta]$ are defined elsewhere [10]. Equation (5) can be written in state space:

$$\{\dot{\chi}\} = [A]\{\chi\}, \qquad \{\chi\} = \{g, \dot{g}\}^T \tag{7}$$

where

$$[A] = \begin{bmatrix} 0 & I \\ -M^{-1}\Omega & -M^{-1}\Delta \end{bmatrix} \tag{8}$$

To obtain the dynamic responses in the present analysis, the first two modes are pulsed separately using the unsteady aeroelastic FUN3D code. This results in a time history of the loads at each body station. A variety of pulses have been used. Marques and Azevedo [25] investigate the use of a unit sample, discrete step and Gaussian pulse. They find that for a nonlinear CFD solver the Gaussian pulse produces the most accurate response for a given time-step size. Figure 2 shows the Gaussian pulse used here. In the present approach, line loads at N_{ll} body stations and N_t time steps are obtained from the FUN3D solution. This results in a rather large set of data. To reduce the data storage required, a proper orthogonal decomposition (POD) of the unsteady line-load data is performed.

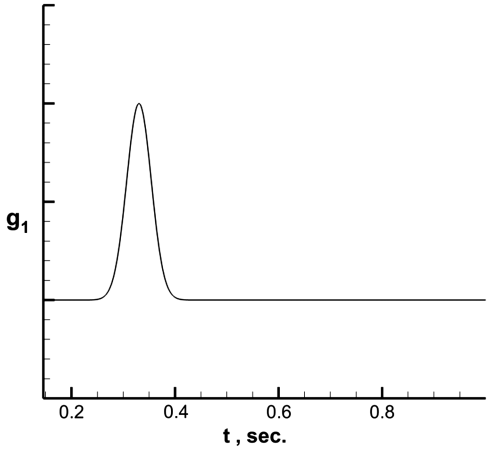

Fig. 2 Gaussian pulse applied to mode 1.

The POD method was originally formulated to study atmospheric turbulence [26] and later to study near-wall turbulence [27]. Subsequently, the POD method has been applied to aeroelastic systems [28]. Here, the reconstructed x-direction line load is derived from

$$\{C_x\}_l = [\Phi_{x\text{POD}}]\{\psi_x\}_l \tag{9}$$

where $[\Phi_{x\text{POD}}]$ is an $N_{ll} \times N_{\text{POD modes}}$ dimension matrix of POD eigenvectors, containing the spatial variation of the response along the vehicle axis. $\{\psi_x\}_l$ is an $N_{\text{POD modes}}$ dimension array of coefficients associated with the x-direction line loads at time step l. Note that the steady values have been removed from the line loads at each body station. The coefficients $\{\psi_x\}_l$ for $l = 1 \rightarrow N_t$ are obtained from a least-squares analysis of an assembly of Eq. (9) for all time steps. The POD modes are the eigenvectors of the $N_{ll} \times N_{ll}$ matrix $[C_x][C_x]^T$. The eigenvectors measure the relative contribution of each body station to the unsteady energy of the mode, whereas the eigenvalues are a relative measure of the energy content of each mode. A limited number of highest-energy modes is typically required to relatively accurately reproduce the data. This procedure is repeated for the line loads in each coordinate direction.

The advantage of using unsteady line loads due to the modal excitation of the first few modes is that they can be used to compute the projection of those responses to an arbitrarily chosen set of additional modes. Other analyses may alternately require rigid-body modes and/or control system modes. Any or all of these can be added (in a quasi-steady sense) to the fully unsteady modes. The generalized aerodynamic stiffness $[Q_k]$, damping $[Q_\zeta]$ and apparent mass $[Q_m]$ can be divided into that due to unsteady and that due to quasi-steady aerodynamics,

$$[Q_k] = \begin{bmatrix} (Q_k)_{\text{dd}} & (Q_k)_{\text{sd}} \\ (Q_k)_{\text{ds}} & (Q_k)_{\text{ss}} \end{bmatrix}, \qquad [Q_\zeta] = \begin{bmatrix} (Q_\zeta)_{\text{dd}} & (Q_\zeta)_{\text{sd}} \\ (Q_\zeta)_{\text{ds}} & (Q_\zeta)_{\text{ss}} \end{bmatrix}$$
$$[Q_m] = \begin{bmatrix} (Q_m)_{\text{dd}} & (Q_m)_{\text{sd}} \\ (Q_m)_{\text{ds}} & (Q_m)_{\text{ss}} \end{bmatrix} \tag{10}$$

where $(\,)_{\text{dd}}$ represents the terms due to the unsteady modal excitation, $(\,)_{\text{ds}}$ is due to projection of the unsteady responses on the quasi-steady modes. Terms $(\,)_{\text{sd}}$ and $(\,)_{\text{ss}}$ are derived exclusively from quasi-steady line-load data. The terms $(\,)_{\text{dd}}$ are derived from a system identification. In this paper the Roger approximation is used, although any method of system identification can be used. It is possible perform the following simulation using the results of the POD analysis, but the Roger approximation readily provides the aerodynamic mass, damping and stiffness terms that are compatible with the quasi-steady analysis as already formulated. To obtain the Roger approximation, the steady-state mean value is removed from the generalized force–time history. The fast Fourier transform (FFT)

of the generalized force–time history is computed, denoted by $\hat{G}$. If the Fourier transform of the generalized forces can be written

$$\{\hat{G}\} = [\hat{Q}]\{\hat{g}\}, \qquad [\hat{Q}] = \begin{bmatrix} (\hat{Q})_{dd} & (\hat{Q})_{sd} \\ (\hat{Q})_{ds} & (\hat{Q})_{ss} \end{bmatrix} \tag{11}$$

then the unsteady aerodynamic submatrix can be modeled

$$[(\hat{Q})_{dd}] = [(A_0)_{dd}] + [(A_1)_{dd}]ik - [(A_2)_{dd}]k^2 + [d]\left[\frac{ik}{ik-\gamma}\right][e] \tag{12}$$

and quasi-steady terms $(\,)_{ds}$ can be modeled,

$$[(\hat{Q})_{ds}] = [(A_0)_{ds}] + [(A_1)_{ds}]ik \tag{13}$$

Having these defined the association can be made $(Q_k)_{dd} = (A_0)_{dd}$, $(Q_\zeta)_{dd} = (A_1)_{dd}$, and $(Q_m)_{dd} = (A_2)_{dd}$. The quasi-steady terms in Eq. (13) derive from the projection of the unsteady line-load data of modes $(\,)_{dd}$ on higher-frequency mode shapes. The remaining terms in Eq. (12) derive from N_R aerodynamic lag states associated with the $(\,)_{dd}$ generalized forces. The coefficients d are preselected so that the lags are distributed equally and in equal numbers between all the modes. The calculation of the terms A_0, A_1, A_2, and e is performed using the method of least squares, while an outer loop attempts an optimization of the lag roots γ. The remaining terms in Eq. (10) are due to quasi-steady aerodynamics. When the complete system of equations is assembled, a stability analysis can be performed to determine the overall damping of the flexible vehicle in flight.

III. CFD and Structural Models

The unstructured tetrahedral mesh is created using VGRID [29]. In the present analysis a grid having 19 million nodes was used. A more complete description of this grid is found in [30]. The structural model used in the Ares I analyses are MSC.Nastran™ finite element models, including the first stage, first-stage solid propellant, upper stage including liquid fuel and oxidizer masses, the Crew Exploration Vehicle (CEV) and Launch Abort System (LAS). The Ares I structural model incorporates a TOI. The TOI is a dual-plane isolation system intended to isolate the CEV from thrust oscillation. The isolator mechanism was modeled by a circumferential ring of springs at the interface between the Orion and the upper stage and by a circumferential ring of spring elements and mass elements at the interface between the upper stage and the first stage.

The entire Ares I vehicle structural model was reduced to 51 points along the vehicle centerline by a Guyan reduction and translational and rotational modal deflections were obtained. Mode shapes having only axial or rotational deflections were discarded. The remaining modes were ranked by the moduli of the mode shape amplitude and the top 37 flexible modes for the Ares I were retained. The y and z translational deflections of the remaining modes were projected with a spline fit to the CFD surface mesh points.

IV. Dynamic Aeroelastic Results

Previous aeroelastic results of the Ares I CLV at Mach 1 and $\alpha = 0$ deg have shown that the FRILLS and the time-accurate CAE analyses differed primarily in the aerodynamic damping of the first two modes (see Fig. 1). The fact that only the first two modes are strongly influenced by unsteady aerodynamics suggests a partitioning in which the first two modes make up the $(\,)_{dd}$ submatrix (modeled fully unsteady) and the $(\,)_{sd}$ and $(\,)_{ss}$ submatrices are modeled in a quasi-steady sense. The unsteady line-load data for the first two modes were obtained by performing time-accurate solutions with FUN3D, pulsing each of modes 1 and 2 separately using the Gaussian pulse shown in Fig. 2. The FUN3D generated line loads at each time step were the data used in the following analyses.

A study using generalized force–time histories was first performed to assess the accuracy of the response to the Gaussian pulse excitation at different time-step sizes. The generalized force–time history used here was derived by projecting the unsteady line loads onto the first mode. The projection involved integrating line loads and modal data at 1000 body stations and over 4000 time steps. Figure 3 shows the FFT of the generalized force (mode 1) due to mode 1 excitation at three time-step sizes, $\Delta t = 5$, 10, and 20. As can be seen in the figure both the real and imaginary responses at all frequencies are converging as the time-step size is reduced. The response at all frequencies using $\Delta t = 10$ is nearly identical to that using $\Delta t = 5$. On the other hand, all the results are nearly identical at low frequencies. Since the accuracy of the low-frequency response is the primary objective, the solution at $\Delta t = 20$ was considered sufficiently accurate.

Since the line-load data at each time step and body station was a rather unwieldy data set, a POD analysis was performed to reduce the data size. Performing several POD analyses with different numbers of POD modes, it was found that a very accurate model of the line loads can be achieved with $N_{\text{POD modes}} = 8$. As seen in Fig. 4, with this number of POD modes, the original and reconstructed generalized force responses are indistinguishable. The POD analysis thus provides a large reduction in the amount of storage required to model the data. As mentioned earlier, the POD eigenvectors provide the relative contributions of each body station to the overall energy of the mode. A composite of the combined highest-energy POD mode amplitudes provides the overall distribution of the unsteady energy over the entire body. To compare the energy distribution from the time-accurate FUN3D line loads and that due to the FRILLS analysis, a similar Gaussian pulse and response was performed using the FRILLS solver. The process to obtain the line-load response from the FRILLS solver was identical to that used for unsteady FUN3D line loads, except the FRILLS solver uses steady-state rigid aerodynamics. Figure 5 shows the composite distribution of the highest-

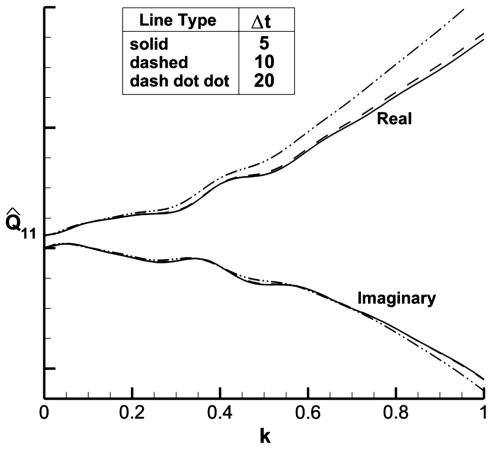

Fig. 3 Time-step study of unsteady Gaussian pulse response (mode 1 on mode 1).

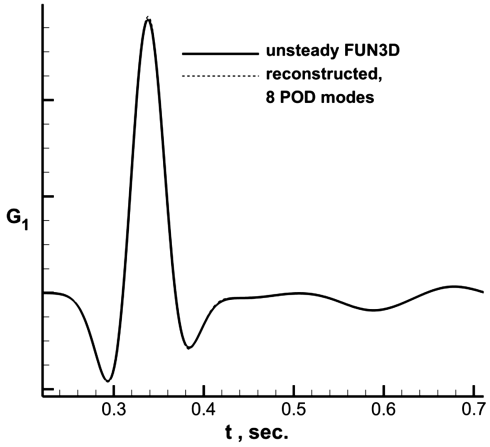

Fig. 4 Comparison of FUN3D and POD approximation of unsteady mode 1 response (the reconstructed solution is from unsteady line loads).

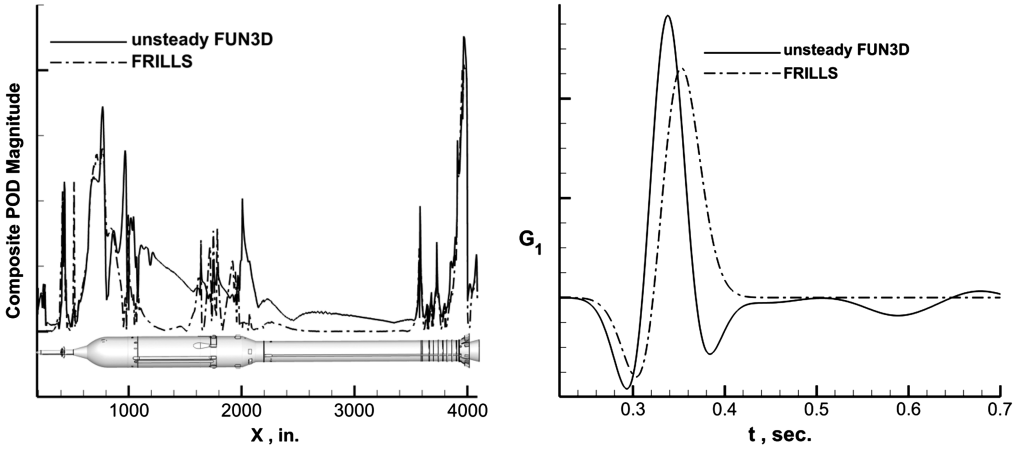

a) Inline load POD eigenvectors b) Generalized force 1

Fig. 5 Comparison of unsteady FUN3D and FRILLS responses due to first-mode Gaussian pulse.

energy POD modes from the unsteady line-load model and that from the quasi-steady FRILLS line loads. That figure clearly indicates that points along the body at which there is a change in cross-sectional area or at major clusters of protuberances the FRILLS and the unsteady FUN3D responses are nearly identical. These areas are at the LAS nozzles, the CEV module and fairing, the upper-stage cluster of protuberances, the first-stage rings and the aft skirt. However, the time-accurate modeling of the unsteady line loads also has high-energy content at locations away from cross-sectional area changes. These areas include the long unchanging region of the upper stage and the first-stage SRB. This indicates that a fully time-accurate solution is required to capture all of the unsteady energy. It also shows that a quasi-steady model only provides energy content at points of geometry change, whereas unsteady energy is in fact distributed both at and away from cross-sectional area changes. It is also note worthy that the frustum dynamics due to the time-accurate solution is much larger than that due to the FRILLS analysis. Also shown in that figure are the generalized force responses integrated from the line loads. The difference in the unsteady and quasi-steady responses is clearly seen in that figure.

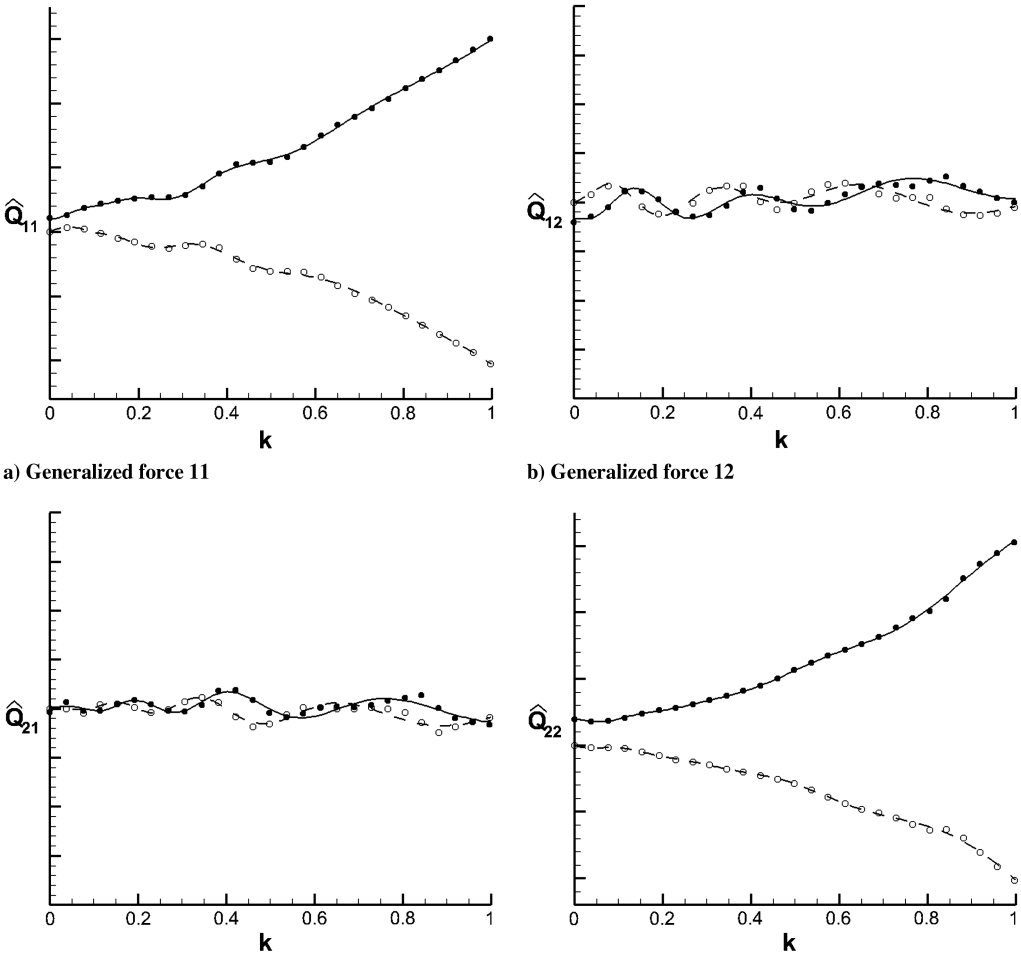

a) Generalized force 11 b) Generalized force 12

c) Generalized force 21 d) Generalized force 22

Fig. 6 FFT of generalized force (filled symbol: real, open symbol: imaginary) and 20-state Roger approximation (line) versus frequency. Data reconstructed from unsteady line loads.

Having a POD model of the unsteady line loads due to an excitation of the first two modes, the following steps were taken to create a state-space model of the flexible launch vehicle. The $(\,)_{ss}$ modes (rigid-body or higher-frequency flexible) to be included in the quasi-steady analysis are chosen. The unsteady line loads due to excitation of the fully dynamic modes, the $(\,)_{dd}$ subset, are projected at each time step to each of the quasi-steady modes. This produces a generalized force–time history of all modes due to excitation of the $(\,)_{dd}$ subset of modes. An FFT analysis was performed on the generalized force responses integrated from the line loads. A Roger approximation using Eq. (12) is calculated for the $(\,)_{dd}$ subset: in this case, the first two modes. A Roger approximation using Eq. (13) is calculated for the $(\,)_{ss}$ subset: in this case, modes 3–37. This produces the $(\,)_{ds}$ submatrices. The $(\,)_{sd}$ and $(\,)_{ss}$ submatrices are derived using quasi-steady FRILLS line-load data. The computation of these submatrices is no different than for a purely quasi-steady FRILLS analysis.

Figure 6 shows the FFT of the generalized force submatrix $(\hat{Q})_{dd}$ (from modes 1 and 2) and the Roger approximation of that data as a function of reduced frequency. The Roger approximation has 10 unsteady aerodynamic states per mode (i.e., $N_R = 20$). With this large number of lag states, quad accuracy (real $*$ 16) was required in the computer code to get meaningful answers. From lifting surface experience this Roger approximation is a quite large number of lag states per mode. However, it should be noted that this is a launch vehicle with rather complex unsteady aerodynamics caused by shock movement, shock separation, and three-dimensional flow separation over various parts of the vehicle. Quite simply, this number of states was required to get the level of accuracy shown in the following results.

The flowfield complexity likely contributes to the complex variation with frequency of the FFT's of the first two modes, seen in Fig. 6. The Roger approximation simulates that complexity very well. In addition, the accuracy of the reproduced time history of the mode 1 generalized force confirms the accuracy of the present model. In Fig. 7, this result is compared with the generalized force–time history of mode 1 obtained directly from the FUN3D modal pulse solution. The Roger model reproduces the original data very accurately up to 0.55 s. Although a slight deviation can be seen in the last 0.10 s of the simulation, the overall agreement is excellent.

Having verified that the POD, FFT, and Roger models all accurately reproduce the data, the model is applied to the aeroelastic simulation of the Ares I. The modified state-space model is solved that includes the lag states ξ, given by

$$\{\dot{\chi}\} = [A]\{\chi\}, \qquad \{\chi\} = \{g, \dot{g}, \xi\}^T \tag{14}$$

where

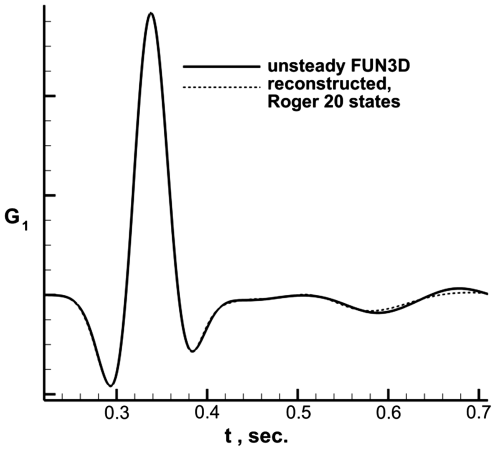

Fig. 7 Time history of response (the reconstructed solution is derived from unsteady line loads).

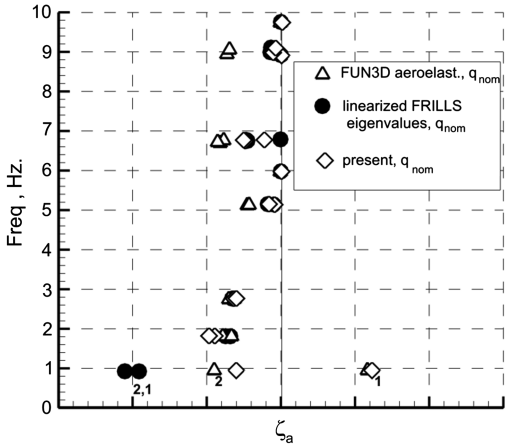

Fig. 8 Frequency versus damping, q_{nom}.

$$[A] = \begin{bmatrix} 0 & I & 0 \\ -M^{-1}\Omega & -M^{-1}\Delta & M^{-1}q_\infty d \\ 0 & e & \gamma \end{bmatrix} \tag{15}$$

Since the interest here is to provide a method useful for time domain simulations of the launch vehicle ascent, time-marching solutions of Eq. (14) were performed. The integration was done with a third-order Euler backward difference. To ensure the accuracy of the solutions, the time step was sized to give 1000 time steps per first-mode period. System damping was extracted by a least-squares log decrement of the entire time traces of the generalized variables. To assess the convergence and accuracy of the log decrement, simulations were performed to 6, 19 and 39 first-mode cycles for several dynamic pressures up to $1.32q_{\text{nom}}$. It was found that the mean (computed from the different length solutions) and standard deviation (computed from successive oscillation cycles) of the first-mode damping each varied at most by 4–5% of the structural damping value. Figure 8 shows the damping of the first 14 modes as a function of frequency at nominal dynamic pressure. The FRILLS and unsteady FUN3D data are presented for reference. The present model significantly improves the overall damping of modes 1 and 2 compared with the FRILLS solution. The first-mode undamping is now captured very well. The second mode is much less strongly damped than in the FRILLS result, although also slightly less damped than the unsteady FUN3D result.

Figure 9 zooms in on the damping of modes 1 and 2 at dynamic pressures q_{nom} and $1.32q_{\text{nom}}$. The unsteady FUN3D dampings at q_{nom} from [10] are also shown. The present state-space model accurately reproduces the continued undamping of mode 1 and increased damping of mode 2 with successively higher dynamic pressures. The results of [18] are also shown in that figure. Although

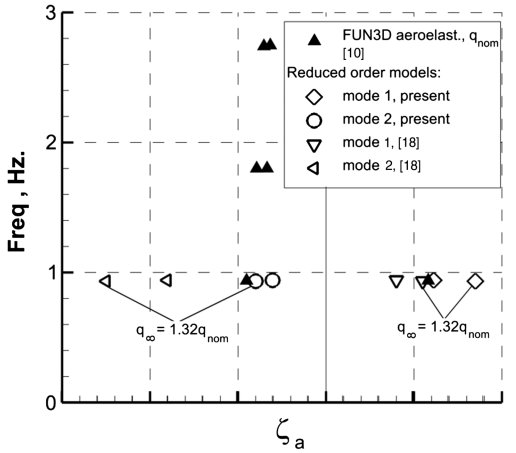

Fig. 9 Frequency versus damping, $q_\infty = q_{\text{nom}}$ and $1.32q_{\text{nom}}$.

the present results are computed from a log decrement of the time domain solution, the damping values from [18] are obtained from an eigenvalue analysis. The standard deviation and variation of the presently computed mean damping discussed above do not explain the difference between the present results and those of [18]. Note that the system identification of [18] is obtained from a step impulse rather than the Gaussian pulse excitation used here. Furthermore, the number of aerodynamic states used in that reference are unknown. It is therefore likely that the improved accuracy of the present results reflects either the number of Roger states used here or the reduced numerical noise of a Gaussian pulse excitation compared with a step impulse.

V. Conclusions

A method has been presented to enhance the quasi-steady method of line loads by using unsteady line-load data for selected modes. For the Ares I vehicle with the thrust oscillation isolator structural model the first two modes are poorly modeled by the quasi-steady method of line loads. Furthermore, these modes are the most likely to couple with rigid-body modes and lead to potential controllability issues. In the present paper a Gaussian pulse is applied to the first two vehicle bending modes and a time history of the line-load response is acquired. Proper orthogonal decomposition is used to reduce the volume of line-load data. The Roger approximation is then used to derive a state-space model that can be incorporated into the quasi-steady line-load model. The results of this study can be summarized. The method of dividing the aeroelastic problem into fully unsteady and quasi-steady partitions has yielded a relatively efficient way of introducing unsteady aerodynamics because a limited number of CFD pulse/response solutions are required. Proper orthogonal decomposition of the time history of the line-load data has successfully reduced the data required for an accurate unsteady aerodynamic model. The time history of the unsteady line loads provides additional insight into the flow physics not available from the integrated generalized forces alone.

One aspect of this method not investigated here is the addition of rigid-body modes, or alternate higher-frequency modes in a quasi-steady sense. Addition of these modes in a quasi-steady sense should be easy, since doing so involves retracing only a few of the steps in the method outlined above and does not involve additional unsteady CFD system identification solutions. The pulse shape used here was a Gaussian pulse of each of the first two modes separately. The use of other pulse functions or the excitation of all modes (in this case, modes 1 and 2) simultaneously was not investigated. Finally, the Roger approximation was used to create the state-space model of the unsteady aerodynamics. Future examination of other time domain methods of system identification would be helpful.

References

[1] Hall, R. M., Holland, S. D., and Blevins, J. A., "Aerodynamic Characterization of a Modern Launch Vehicle," AIAA Paper 2011-10, Jan. 2011.

[2] Ericsson, L. E., "Aeroelastic Instability Caused by Slender Payloads," *Journal of Spacecraft and Rockets*, Vol. 4, No. 1, 1967, pp. 65–73. doi:10.2514/3.28811

[3] Ericsson, L. E., and Pavish, D., "Aeroelastic Vehicle Dynamics of a Proposed Delta II 7920-10L Launch Vehicle," *Journal of Spacecraft and Rockets*, Vol. 37, No. 1, 2000, pp. 28–38. doi:10.2514/2.3546

[4] Ericsson, L. E., "Unsteady Flow Separation Can Endanger the Structural Integrity of Aerospace Launch Vehicles," *Journal of Spacecraft and Rockets*, Vol. 38, No. 2, 2001, pp. 168–179. doi:10.2514/2.3690

[5] Hanson, P. W., and Doggett, R. V., "Aerodynamic Damping and Buffet Response of an Aeroelastic Model of the Saturn I Block II Launch Vehicle," NASA Technical Note NASA TN D-2713, 1965.

[6] Doggett, R. V., and Hanson, P. W., "An Aeroelastic Model Approach for the Prediction of Buffet Bending Loads on Launch Vehicles," NASA Technical Note NASA TN D-2022, 1963.

[7] Hanson, P. W., and Doggett, R. V., "Aerodynamic Damping of a 0.02-Scale Saturn SA-1 Model Vibrating in the First Free-Free Bending Mode," NASA Technical Note NASA TN D-1956, 1963.

[8] Azevedo, J. L. E., "Aeroelastic Analysis of Hammerhead Payloads," AIAA Paper 1988-2307, 1988.

[9] Reding, J. P., and Ericsson, L. E., "Effect of Aeroelastic Considerations on Seasat-A Payload Shroud Design," *Journal of Spacecraft and Rockets*, Vol. 18, No. 3, 1981, pp. 241–247. doi:10.2514/3.57810

[10] Bartels, R., Chwalowski, P., Massey, S., Heeg, J., and Mineck, R., "Computational Aeroelastic Analysis of the Ares I Launch Vehicle During Ascent," *Journal of Spacecraft and Rockets* (submitted for publication).

[11] Trikha, M., Mahapatra, D. R., Gopalakrishnan, S., and Pandiyan, R., "Analysis of Aeroelastic Stability of a Slender Launch Vehicle using Aerodynamic Data," AIAA Paper 2008-310, Jan. 2008.

[12] Azevedo, J. L. E., "Aeroelastic Analysis of Launch Vehicles in Transonic Flight," *Journal of Spacecraft and Rockets*, Vol. 26, No. 1, 1989, pp. 14–23. doi:10.2514/3.26027

[13] Bigarella, E. D. V., Basso, E., and Azevedo, J. L. E., "Multigrid Adaptive-Mesh Turbulent Simulations of Launch Vehicle Flows," AIAA Paper 2003-4076, June 2003.

[14] Bigarella, E. D. V., and Azevedo, J. L. E., "Numerical Study of Turbulent Flows over Launch Vehicle Configurations," *Journal of Spacecraft and Rockets*, Vol. 42, No. 2, 2005, pp. 266–276. doi:10.2514/1.6889

[15] Scalabrin, L. C., and Azevedo, J. L. E., "Finite Volume Launch Vehicle Flow Simulations on Unstructured Adaptive Meshes," AIAA Paper 2003-601, Jan. 2003.

[16] Scalabrin, L. C., Azevedo, J. L. E., Teixeira, P. R. E., and Awruch, A. M., "Three Dimensional Flow Simulations with the Finite Element Technique over a Multi-Stage Rocket," AIAA Paper 2002-408, Jan. 2002.

[17] Capri, E., Mastroddi, E., and Pizzicaroli, A., "Linearized Aeroelastic Analysis for a Launch Vehicle in Transonic Flight," *Journal of Spacecraft and Rockets*, Vol. 43, No. 1, 2006, pp. 92–104. doi:10.2514/1.13867

[18] Silva, W., Vatsa, V., and Biedron, R., "Reduced Order Models for the Aeroelastic Analysis of the Ares Vehicles," AIAA Paper 2010-4375, June 2010.

[19] Anderson, W. K., and Bonhaus, D. L., "An Implicit Upwind Algorithm for Computing Turbulent Flows on Unstructured Grids," *Computers and Fluids*, Vol. 23, No. 1, 1994, pp. 1–22. doi:10.1016/0045-7930(94)90023-X

[20] *FUN3D Manual*, NASA Langley Research Center, Hampton, VA, Nov. 2008.

[21] Spalart, P. R., and Allmaras, S. R., "One-Equation Turbulence Model for Aerodynamic Flows," AIAA Paper 1992- 439, Jan. 1992.

[22] Vatsa, V. N., and White, J. A., "Calibration of a Unified Flux Limiter for Ares-Class Launch Vehicles from Subsonic to Supersonic Speeds," *56th JANNAF Propulsion Meeting*, 2009.

[23] Nielsen, E. J., Lu, J., Park, M. A., and Darmofal, D. L., "An Exact Dual Adjoint Solution Method for Turbulent Flows on Unstructured Grids," *Computers and Fluids*, Vol. 33, No. 9, 2004, pp. 1131–1155. doi:10.1016/j.compfluid.2003.09.005

[24] Samareh, J. A., "Discrete Data Transfer Technique for Fluid-Structure Interaction," AIAA Paper 2007-4309, June 2007.

[25] Marques, A. N., and Azevedo, J. L. E., "Application of CFD-Based Unsteady Forces for Efficient Aeroelastic Stability Analyses," AIAA Paper 2006-250, Jan. 2006.

[26] Lumley, J. L., "The structure of inhomogeneous turbulent flows," *Atmospheric Turbulence and Radio Wave Propogation*, edited by A. M. Yaglom, and V. I. Tatarski, Nauka, Moscow, 1967, pp. 166–178.

[27] Berkooz, G., Carlson, H., Holmes, P., and Lumley, J. L., "Progress in understanding the dynamics of coherent structures in the wall layer," *Near-Wall Turbulent Flows*, edited by R. M. C. So, C. G. Speziale, and B. E. Launder, Elsevier, Amsterdam, 1993, pp. 1–21.

[28] Carlson, H. A., Feng, J. Q., Thomas, J. P., Kielb, R. E., Hall, K. C., and Dowell, E. H., "Computational Models for Nonlinear Aeroelasticity," AIAA Paper 2005-1085, Jan. 2005.

[29] Pirzadeh, S. Z., "Advanced Unstructured Grid Generation for Complex Aerodynamic Applications," AIAA Paper 2008-7178, June 2008.

[30] Bartels, R., Vatsa, V., Carlson, J.-R., Park, M., and Mineck, R., "FUN3D Grid Refinement and Adaptation Studies for the Ares Launch Vehicle," AIAA Paper 2010-4372, June 2010.

S. P. Pao
Associate Editor